Journal of Materials Chemistry A

Ligand Environment Engineering of Nickel Single Atomic Sites for Efficient Electrochemical Carbon Dioxide Reduction Reaction

Journal:	*Journal of Materials Chemistry A*
Manuscript ID	TA-ART-09-2024-006720.R1
Article Type:	Paper
Date Submitted by the Author:	11-Dec-2024

Complete List of Authors:	Kim, Min Sung; Kyungpook National University, Materials Science and Engineering Priyadarsini, Adyasa; Florida A&M University, Physics Lee, Ju-Hyeon; Kyungpook National University, Materials Science and Engineering Bae, Jin-Gyu; Kyungpook National University, Materials Science and Engineering Heo, Jeong Yeon; Kyungpook National University, Materials Science and Engineering Lee, Hyeon Jeong; Ulsan National Institute of Science and Technology, Materials Science and Engineering Kattel, Shyam; University of Central Florida, Physics Lee, Ji Hoon; Kyungpook National University, School of Materials Science and Engineering

Journal of Materials Chemistry A Paper

Ligand Environment Engineering of Nickel Single Atomic Sites for Efficient Electrochemical Carbon Dioxide Reduction Reaction

Received 00th January 20xx,
Accepted 00th January 20xx

DOI: 10.1039/x0xx00000x

Min Sung Kim,‡[ab] Adyasa Priyadarsini,‡[c] Ju-Hyeon Lee,[ab] Jin-Gyu Bae,[ab] Jeong Yeon Heo,[ab] Hyeon Jeong Lee,[d] Shyam Kattel,*[e] and Ji Hoon Lee,*[ab]*

Electrochemical carbon dioxide reduction reaction (CO_2RR) is considered one of the feasible options for a net reduction of CO_2 emission, especially when coupled with renewable energy resources. Many techno-economical assessments on CO_2RR have concluded that the production of syngas (CO/H_2), a precursor for Fischer–Tropsch synthesis, is beneficial. Thus, cost-effective and durable catalysts are needed to selectively promote the CO_2RR to produce syngas. Ni-based single-atom catalysts (Ni-SACs) have gained significant interest for CO_2RR to syngas conversion. However, there is still a lack of understanding of the physicochemical properties of isolated Ni atomic sites with different ligand environments and the resultant CO_2RR performance. In this study, we combined experimental measurements, *in-situ* X-ray absorption fine structure analyses, and density functional theory calculations to study a series of Ni-SACs with controlled Ni configuration and N-coordination and revealed that Ni–N_x sites with less than 4 N coordination are the catalytic active sites for the selective CO_2RR process. This study provides fundamental insights into the rational design for Ni-SACs toward the enhanced CO_2RR activity and selectivity based on their structure-property relationship.

1 Introduction

Recently, single atom catalysts (SACs) have received considerable attention in both scientific and technical areas because of their extraordinary properties originating from the atomically-dispersed catalytic active sites. SACs have demonstrated their promise in various thermo-/electro-catalysis applications.[1-4] The high catalytic performance of SAC originates mainly from the unsaturated coordination chemical environments of the catalytic active center that provide not only excellent chemical stability due to the strong chemical bonding between single atoms and substrates but also exhibit unique but beneficial binding configurations and energies of reaction intermediates compared with the bulk catalyst counterparts. Along with this direction, manganese (Mn), iron (Fe), cobalt (Co), nickel (Ni), copper (Cu), rhodium (Rh), palladium (Pd), iridium (Ir), and platinum (Pt) with single atomic sites has been widely investigated as electrocatalysts for oxygen reduction/evolution reactions, hydrogen evolution/oxidation reactions, alcohol oxidation reaction, and carbon dioxide reduction reaction (CO_2RR).[5-22] Among them, it was found that the Ni single atomic sites covalently-coordinated by nitrogen defects on the porous carbon supports,[23-25] so-called Ni-SACs, demonstrated excellent CO_2RR performance toward carbon monoxide (CO) production such as high Faradaic efficiency (FE), partial current density (J), and good catalytic life span. Despite their outstanding electrocatalytic properties, the physicochemical structure of the catalytic active Ni–N_x moieties and CO_2RR mechanism remain poorly understood. It is likely that the N atoms in Ni–N_x do not determine the catalytic properties but that the CO_2RR performance varies depending on the N-configurations (*e.g.*, pyridine-like N (N-6), pyrrole-like N (N-5), and quaternary N (N-Q), *etc.*), their coordination to Ni (*i.e.*, Ni–N_x, x = 2~4), and their electronic properties.[26-28] However, a clear understanding and chemical identification of active Ni–N_x sites on carbon support and a structure-activity/selectivity relationship of Ni–N_x for CO_2RR remains elusive.

In this study, we systematically investigated the dependence of CO_2RR performance on the N-ligand environments of Ni-SACs, controlled by synthetic conditions to modify the local physicochemical structure around Ni single atomic sites. The X-ray absorption fine structure (XAFS) analysis revealed that, under lower carbonization conditions (*i.e.*, either lower annealing temperature or N_2/Ar gas flow without H_2 gas), the pyridine-like N-6 configuration possessing lone-pair electrons was dominant, with most Ni atoms close to a Ni–N_4 configuration. In contrast, as the degree of carbonization increased (by raising the annealing temperature or employing H_2 gas), the N-6 content decreased, leading to single atomic Ni sites with less than 4 N coordination[24, 29, 30] and eventually resulting in the formation of metallic Ni nanoparticles. Electrochemical evaluation revealed that the CO_2RR activity and selectivity increase as the value of x in the Ni–N_x decreases from 4 (*i.e.*, with less than 4 N coordination). Our optimal Ni-SAC (x ≈ 2.9 in the Ni–N_x moiety) exhibited superior FE and J values for CO evolution (*e.g.*, FE_{CO}=91% and J_{CO}=11.1 mA cm_{geo}^{-2} at –0.8 V vs. reversible hydrogen electrode (V_{RHE})) without any activity loss during long-term operation. Density functional theory (DFT) calculations performed on N-doped graphene layers containing the Ni single atom sites identified that both Ni configuration (*e.g.*, single-, double-, and triple-vacancies) and N coordination play an important role in enhancing CO_2RR over hydrogen

[a] School of Materials Science and Engineering, Kyungpook National University, Daegu 41566, Republic of Korea. E-mail: jihoonlee@knu.ac.kr
[b] KNU Advanced Material Research Institute, Kyungpook National University, Daegu 41566, Republic of Korea
[c] Department of Physics, Florida A&M University, Tallahassee, FL 32307, United States
[d] Department of Materials Science and Engineering, Ulsan National Institute of Science and Technology, Ulsan 44919, Republic of Korea. E-mail: hyeonjeong.lee@unist.ac.kr
[e] Department of Physics, University of Central Florida, Orlando, FL 32816, United States. E-mail: shyam.kattel@ucf.edu
† Electronic supplementary information (ESI) available. See DOI: 10.1039/x0xx00000x
‡ These authors contributed equally to this work.

evolution reaction (HER), its competing reaction, with the Gibbs free energy difference of *COOH and *H being a good descriptor for predicting the CO_2RR activity and selectivity.

2 Experimental

2.1 Synthesis of a series of Ni-SACs

All chemicals were purchased from Aldrich and utilized without further purification unless stated otherwise. Glucose (5 g) and dicyandiamide (0.25 g) were dissolved in deionized water (DI water, 100 mL, >18.0 MΩ), followed by the addition of 2 mL of nickel chloride hexahydrate solution (0.0125 M). The mixture was heated at 80 °C with vigorous stiring to evaporate DI water, and the solid product was intimately ground to be a precursor for Ni-SACs. The series of Ni-SACs were synthesized by stabilization and carbonization steps of the precursors. The stabilization step was performed at 200 °C for 2 h under a 200 sccm dry air flow to stabilize the N-containing precursor, followed by the carbonization step performed for 1 h at different temperatures (either 700, 800, or 900 °C) and Ar-balanced atmospheres (i.e., Ar/N_2 = 50 sccm/50 sccm or $Ar/N_2/H_2$ = 40 sccm /40 sccm /20 sccm). Both annealing steps were performed at a heating rate of 4 °C min^{-1}. The final samples were denoted as Ni-SAC-T/g, where T and g refer to carbonization temperature (denoted as 700, 800, and 900 °C) and gas atmosphere (denoted as Ar (=Ar/N_2) and H_2 (=$Ar/N_2/H_2$)), respectively.

2.2 Electrochemical evaluation

For working electrode (WE) fabrication, 8 mg of the catalyst was first dispersed in a mixture of DI water (1.1 mL) and ethanol solution (0.6 mL) containing 5 wt% Nafion solution (0.3 mL) at a concentration of 4 $mg_{Ni\text{-}SAC}$ mL^{-1}. The homogeneous catalyst ink was prepared with ultrasonication for 30 min. Then, 100 μL of the homogeneous ink was dropped and dried on 1 cm^2 of the carbon current collector (1 cm × 2 cm, TGP-H-060, 5% water-proofed, Toray Corp.). The areal mass loading of Ni-SAC (0.4 $mg_{Ni\text{-}SAC}$ cm^{-1}) was confirmed using a microbalance (XPR106, readability = 2 μg, Mettler Toledo). The electrolyte was 0.5M potassium bicarbonate ($KHCO_3$) aqueous solution, prepared by bubbling high-purity CO_2 gas (99.99%) for 12 h into 0.25M potassium carbonate (K_2CO_3, >99.995%) aqueous solution. We note that, prior to any CO_2RR experiments, both catholyte and anolyte were further purified by electrolysis between two graphite rods (Alfa Aesar) at 1.5 V to remove any trace amount of metallic species until reaching a constant current (< ~100 μA).

The electrochemical experiments were run at 25 °C in a three-electrode configuration with a vigorous stirring and continuous CO_2 flow. A high-resolution workstation (BioLogic, SP-150-e) was employed to record the electrochemical signal. To avoid undesired side-reaction from the platium-containing species, graphite rod and hydrogen electrode (EDAQ, Hydroflex ET070) were used as the counter electrode (CE) and reference electrode (RE), respectively. The usage of the hydrogen electrode set the WE potential to be a RHE scale. The gastight two-compartment H-type cell filled with CO_2-saturated 0.5M $KHCO_3$ solution was used as a reactor. Each compartment contained 30 mL of electrolyte, separated by proton exchange membrane (Nafion 117). The WE and RE were placed in the cathodic compartment while the CE was placed in the anodic compartment. The WE potential was controlled by iR-compensation (80%) to compensate for solution resistance (R_s), which was typically in the range of 13–15 Ω cm^{-2}. The R_s value was obtained in the Nyquist plot. Electrochemical impedance spectroscopy (EIS) was performed in the frequency range of 1 MHz to 0.1 Hz with an AC signal of 10 mV. Nyquist plots were fitted using an electrochemical equivalent circuit consisting of solution resistance (R_s), charge transfer resistance (R_{CT}), and constant phase element (Q_{CT}). Electrochemical surface area (ECSA) values for Ni-SACs were determined by electrical double layer capacitance (EDLC) measurements, assuming a unit areal capacitance of 21 μF cm^{-2}.[18] The EDLC was calculated from the slope in a plot of the current density at 0.02 V_{RHE} as a function of applied scan rates.

The electrochemical CO_2RR performance (*i.e.*, FE and J) was evaluated by using the chronoamperometry (CA) technique at each constant potential for ~2.7 h. During the CO_2RR, CO_2 was continuously delivered into the cathodic compartment at a flow rate of 20 sccm and gaseous products were directly vent into the gas sampling loop of a gas chromatograph (GC, DS Science, iGC7200) with ultrahigh pure Ar gas (99.999 %) as the carrier gas. The GC was set to collect the gas products every 1650 s. The gas products were quantified by a thermal conductivity detector and flame ionization detector, where H_2 and CO were quantified, respectively. Partial FE (%) and J (mA cm_{geo}^{-2}) values toward CO and H_2 were calculated by the following equations (1) and (2):

(1) J_{CO} (or J_{H2}) = C(CO) (or C(H_2)) × Q × 2 × F ÷ V_M ÷ A

(2) FE_{CO} (or FE_{H2}) = J_{CO} (or J_{H2}) ÷ J_{total} × 100

where C(CO)/C(H_2) refers to the concentration of CO/H_2 determined from GC analyses, Q is the flow rate of CO_2 into the cell (20 sccm), confirmed by a universal flow meter (ADM flow meter, Agilent, G6691), F is the Faradaic constant (96485 C mol^{-1}), V_M is 22.4 L mol^{-1}, and A is the electrode area (1 cm^2). J_{total} was calculated by integrating the CA curve over the time for the given GC cycle. FE and J values for CO and H_2 were calculated by averaging the individual values during six GC sampling sessions. Normalized current densities (*j*, mA μg_{Ni}^{-1} cm^{-2}) were calculated by dividing the J values by the Ni contents in the given electrodes.

CO_2RR experiments were further conducted using a gas diffusion electrode (GDE)-based flow cell reactor. Homogeneous catalyst inks containing Ni-SAC-700/H_2 and Ni-SAC-900/Ar were sprayed onto carbon paper (Sigracet 39BB) and vacuum-dried for 2 h before use as the WE. The areal mass loading of the GDE was controlled to be 1.5 $mg_{Ni\text{-}SAC}$ cm^{-2}. The CE was prepared with IrO_2 (Alfa Aesar) dispersed on Vulkan XC 72 catalysts via the same preparation method as the WE. Both the WE and CE had a geometric area of 4 cm^2. The RE and electrolyte used in the flow cell configuration were identical to

those used in the H-cell setup. A Nafion 117 membrane was placed between the catholyte and anolyte compartments. Electrolytes were circulated at a flow rate of 2 mL min^{-1} using a peristaltic pump (SHENCHEN) from 20 mL reservoirs for both the catholyte and anolyte. Humidified CO_2 gas was supplied to the gas chamber beneath the GDE at a flow rate of 20 sccm. Stability tests were performed for 10 h using the CA method at –0.6 V_{RHE} with continuous circulation of catholyte, anolyte, and CO_2. The other conditions were identical to those in the H-cell configuration tests.

2.3 Characterization

The crystallinity of Ni-SACs was characterized using X-ray diffraction (XRD, Xpert-Pro, PANalytical, Cu Kα = 1.5406 Å). The degree of graphitization of Ni-SACs was characterized using Raman spectroscopy (Ramboss-Star, DongWoo Optron, 532 nm). The typical sample morphology and elemental distribution of Ni-SACs were characterized by high-resolution transmission electron microscopy (HR-TEM, Titan G2, FEI, 200 kV) equipped with a probe Cs-corrector and four windowless silicon drift detectors. High-angle annular dark field scanning TEM (HAADF-STEM) analyses were performed to observe the single atomic distribution of Ni atoms (JEM-ARM300F, JEOL, 300 kV). The Ni content was determined by using inductively coupled plasma optical element spectroscopy (ICP-OES, 7300 DV, Optima). The C, N, and O contents were characterized by combustible elemental analysis (EA, Flash 2000, Thermo Fisher). The chemical environments of the catalysts were investigated using X-ray photoemission spectroscopy (XPS, Thermal Fisher, Nexsa, Al Kα = 1486.6 eV). The obtained spectra were calibrated with C1s binding energy (284.8 eV). The specific surface area (SSA, $m^2\ g^{-1}$), pore volume (V_{pore}, $cm^3\ g^{-1}$), and pore size distribution were obtained from N_2 adsorption/desorption measurements by using a porosity analyzer (Micromeritics 3FLEX, USA) operating at 77 K. Prior to the porosity measurement, each sample was degassed at 130 °C for 24 h. The sample amount was approximately 150 mg. The SSA was calculated based on the Brunauer-Emmett-Teller (BET) method[31] and the pore volume was determined by adsorbed quantity at a relative pressure (P/P_o) of 0.99. Microporosity data (*i.e.*, micropore SSA ($SSA_{micropore}$, $m^2\ g^{-1}$), and micropore volume ($V_{micropore}$, $cm^3\ g^{-1}$)) were obtained by t-plot analyses.[32] Pore size distribution was obtained by the non-local density functional theory method assuming slit-shaped pore geometry.

2.4 XAFS analysis

The XAFS measurements were performed on the 10C (Wide XAFS), 8C (Nano XAFS), and 7D (XAFS) beamlines in the Pohang Light Source-II (PLS-II) of Pohang Accelerating Laboratory (PAL), respectively. *In-situ* XAFS analyses at Ni K-edge were conducted to compare the XANES profiles of Ni-SAC containing WEs at the pristine state and during CO_2RR at –0.6 V_{RHE}. The lab-made acryl kit was used for *in-situ* XAFS analysis.[4, 33-35] *In-situ* XAFS measurements were carried out on the 7D beamline equipped with a 7-element Ge detector. The 7-element Ge detector selectively sampled the fluorescence signal corresponding to L_3-K transition (7480.3 eV) from the beam exposure area (3(W) × 1(H) mm^2), thus effectively amplifying the dilute XANES signal originating from the limited Ni contents (≈1.37 μg_{Ni} in this *in-situ* measurement) in the WEs during the CO_2RR. Due to the limited Ni concentration in the Ni-SAC electrode along the X-ray beam path, which resulted in significantly weak oscillations in the high-*k* region of the XAFS spectra, it is challenging to obtain discernible EXAFS data during *in-situ* XAFS analyses. The storage ring was operated in a top-up mode at an energy of 3.0 GeV and an operating current of 250 mA. XAFS spectra were obtained at room temperature under both transmission and fluorescence modes by using a double-crystal monochromator (Si(111)) detuned to 70% of its maximum intensity to avoid unwanted high-order harmonics. The energy of each spectrum was calibrated using the edge energy (E_o) of the Ni foil (8333 eV) that was recorded simultaneously.

X-ray absorption near edge structure (XANES) and extended XAFS (EXAFS) analyses were conducted by using the ATHENA and ARTEMIS software in the IFEFFIT package. Detailed data processing was conducted in accordance with the procedures described in previous reports. The EXAFS spectrum ($\chi(k)$) was weighted by k^3 to intensify the oscillation in the high *k* regime. Amplitude reduction factor (S_o^2) values were obtained by fitting the nickel phthalocyanine (Ni-Pc). The Hanning window was used for Fourier transform (FT) into *R*-space (Å). All EXAFS fittings were performed in *R*-space. The reliable factor (R-factor) and reduced chi-square were used to evaluate the goodness of fit. The Debye-Waller factor (σ^2) value was fixed as the optimal value in the last fitting process step to reduce the number of variables.

2.5 Computational details

Various Ni-SACs with different vacancies and N decoration on a single layer of graphene were modeled. Ni configuration was controlled by creating different vacancy types (*i.e.*, single, double, and triple) and the N decoration was controlled by the number of N substitutes on the graphene layer. All the DFT calculations to optimize the surface and the adsorption of reaction intermediate structures were performed using the Vienna Ab initio Simulation Package (VASP) code.[36] The projector augmented wave (PAW) method[37] was used to describe the interaction between the frozen core and free valence electrons. Perdew-Burke-Ernzerhof (PBE) exchange-correlation functional,[38] within generalized gradient approximation (GGA) along with semiempirical D3 dispersion correction, for van del Waal's interaction, was used for all the calculations.[39, 40] The cut-off energy for structure optimization was set to 450 eV throughout the simulation. We have used a 3 × 4 graphene supercell with 48 atoms to model various Ni–N_x moieties. The periodic images are separated by a 15 Å vacuum along the z-direction to avoid self-interaction errors. A 3 × 3 × 1 Monkhorst-Pack k-point mesh was used to sample the Brillouin

zone. The structural relaxation was performed iteratively until the energy and force criteria converged to 10^{-6} eV and 10^{-2} eV $Å^{-1}$, respectively. The solvation effect in the calculations was included using the method developed by Hening's group (VASPsol).[41] Since our experimental measurements were done in a neutral electrolyte, we used the default relative permittivity of water (*i.e.*, a value of 78.4) for all calculations. The theoretical workflow follows formation energy and binding energy calculations to determine thermodynamically most favorable Ni–N_x configurations.

The formation energy is calculated as,

$$E_{formation} = E_{Ni-N_x} - E_{Ni} - x(E_N) - n(E_C) \quad (1)$$

where E_{Ni-N_x} is the DFT calculated total energy of N coordinated Ni–N_x moiety, E_{Ni} is the energy of Ni atom obtained from the optimized bulk Ni, E_N is the energy of nitrogen atoms calculated as $\frac{1}{2}E_{N_2}$, E_C is the energy of the carbon atom calculated from the graphene unit cell, n is the total C atoms after vacancy formation and N substitution, x is the total N substituting C on the graphene surface.

The binding energy (BE) is calculated as,

$$BE = E_{Ni-N_x} - E_{(Ni-N_x)-Ni} - E_{Ni} \quad (2)$$

where E_{Ni-N_x} is the DFT calculated total energy of N coordinated Ni–N_x moiety and $E_{(Ni-N_x)-Ni}$ is the total energy of the graphene supercell with nitrogen-decorated vacancies without Ni.

We have chosen eight candidates based on the DFT calculated formation energies for reduction reaction calculations, on which the two competing reduction reactions, namely, CO_2RR and HER were studied. The free energy barriers for reaction intermediate adsorption were calculated using the computational hydrogen electrode (CHE) model.[42] Within this approach, the free energy of a proton-coupled electron ($H^+ + e^-$) is equal to the free energy of ½H_2.[43] Along the CO_2RR and HER reaction pathways, the overpotential required to make the whole CO_2RR/HER barrierless is calculated from the step with the highest free energy change/barrier. For CO_2RR, we have considered steps until CO desorption. The free energy barriers for CO_2RR to CO are calculated as follows,

$$* + CO_2 + H^+ + e^- \rightarrow *COOH \quad (R1)$$

$$\Delta G_1 = G_{*COOH} - G_* - G_{CO_2(g)} - G_{\frac{1}{2}H_2(g)} \quad (3)$$

$$*COOH + H^+ + e^- \rightarrow *CO + H_2O \quad (R2)$$

$$\Delta G_2 = G_{*CO} - G_{*COOH} - G_{\frac{1}{2}H_2(g)} + G_{H_2O} \quad (4)$$

$$*CO \rightarrow * + CO(g) \quad (R3)$$

$$\Delta G_3 = G_{CO(g)} + G_* - G_{*CO} \quad (5)$$

Previous calculations have shown that DFT does not accurately capture the energy of CO_2(g) and CO(g). Thus, a correction of +0.13 and –0.51 eV is added to the PBE calculated enthalpy of CO_2(g) and CO(g) molecules, respectively.[44] For HER, the free energy barrier of hydrogen adsorption is considered since H is the only reaction intermediate of HER. We have followed the solvated H^+ as the reactive species instead of dissociative water adsorption on the surface. Following Kehlet and coworkers' work, H adsorption, *i.e.*, the Volmer step, is a reliable descriptor for HER electrocatalyst.[45] Thus, the free energy barrier of HER is calculated as follows,

$$\Delta G_{HER} = G_{*H} - G_* - G_{\frac{1}{2}H_2} \quad (6)$$

For any reaction step (*i*), the change in free energy is calculated as,

$$\Delta G_i = \Delta E_i + \Delta ZPE_i - T\Delta S_i \quad (7)$$

where ΔE_i is the DFT calculated change in energy, ΔZPE_i and $T\Delta S_i$ are zero point and entropic contribution, respectively. The effect of pH is included by adding $k_BT \times \ln 10 \times pH$ (≈ 0.0591×pH) to ΔG values for the steps that involve ($H^+ + e^-$) transfer.[46] Therefore, the free energy change/barrier between two successive steps is given by

$$\Delta G_i(pH) = \Delta G_i + 0.0591 * pH \quad (8)$$

Under this framework, the *CO desorption, a final step of CO_2RR, is a pH-independent step.

The limiting potential of the reduction reaction, U_{PDS}, is calculated from the step with the maximum free energy barrier (ΔG_{max}) as follows,

$$U_{PDS} = \Delta G_{max}/e \quad (9)$$

We have also correlated the adsorbate BEs to the potential determining step (PDS) in order to find which species controls the CO_2RR. The adsorbate binding energy (E_{ads}) is calculated as,

$$E_{ads} = E_{*adsorbate} - E_* - E_{adsorbate} \quad (10)$$

where $E_{*adsorbate}$ is the total energy of the surface adsorbed species, E_* is the total energy of graphene with Ni–N_x moiety, and $E_{adsorbate}$ is the total energy of the adsorbate in the gas phase.

3 Results and discussion

3.1 Material characterizations

We synthesized Ni-SACs by uniformly mixing Ni/N/C-containing precursors, followed by the carbonization process in inert atmospheres. It is well-known that the physicochemical properties of carbonaceous materials are highly sensitive to carbonization conditions, including annealing temperatures and gas conditions.[47, 48] To evaluate the porosity properties, BET analyses were performed for all Ni-SACs. The N_2 adsorption/desorption isotherms at 77 K provided quantitative information on the porosities of the catalysts (Figs. S1 and S2). All catalysts exhibited type IV isotherms (Fig. S1) with a small hysteresis around P/P_o = 0.9, indicating the presence of macropores and mesopores. This observation is further corroborated by the pore size distribution curves (Fig. S2), which show that pores larger than 20 Å contribute predominantly to the total pore volume. Notably, the porosity of Ni-SACs tends to increase with higher heat treatment temperatures and the use of Ar/N_2 gas mixtures. The results reveal that porosity properties, including SSA and V_{pore}, are significantly affected by the carbonization temperature (700, 800, and 900 °C) and gas atmosphere (Ar/N_2 or $Ar/N_2/H_2$). The ECSA values for Ni-SACs generally follow a similar trend to SSA values (Fig. S3), except for Ni-SAC-900/H_2. Despite its high SSA (1631 $m^2\ g^{-1}$), Ni-SAC-900/H_2 exhibits a lower ECSA (77.4 $m^2\ g^{-1}$), likely due to Ni atom agglomeration, as will be discussed in the following XRD section. Among the samples, Ni-SAC-900/Ar exhibited the highest SSA (1926

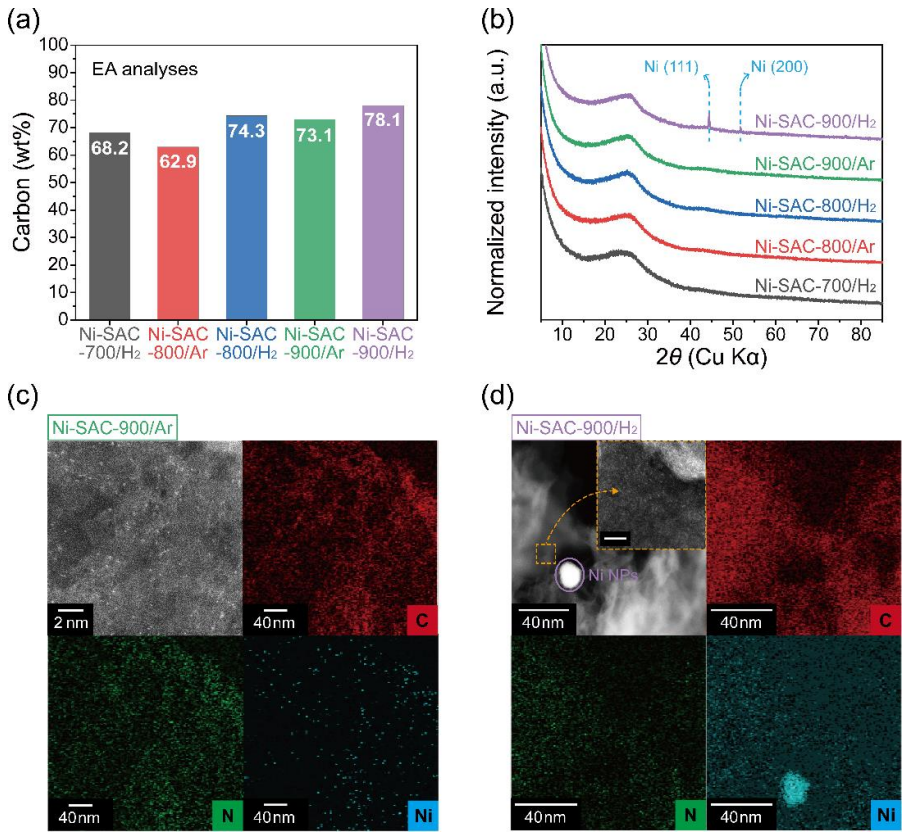

Fig. 1 Structural and chemical analyses of a series of Ni-SACs. (a) EA analyses and (b) XRD patterns of the samples. (c–d) HAADF-STEM images along with the elemental mapping for (c) Ni-SAC-900/Ar and (d) Ni-SAC-900/H_2. The scale bar in the inset in Fig. 1d represents 5 nm.

$m^2\ g^{-1}$), V_{pore} (10 $cm^3\ g^{-1}$), and ECSA (144.4 $m^2\ g^{-1}$).

We evaluated the carbonization degree based on the carbon content (in wt%, Fig. 1a and Table S1) obtained through the combustible EA results, revealing that carbonization was facilitated by the increase in the annealing temperature and the usage of H_2 gas. For instance, Ni-SAC-900/Ar contains approximately 10.2 wt% more carbon than Ni-SAC-800/Ar. And, Ni-SAC-800/H_2 contains approximately 11.4 wt% more carbon than Ni-SAC-800/Ar. Both comparisons indicate that the chemical properties in N-doped carbons varied with the annealing conditions, thereby affecting the properties of the anchored Ni site on the supports. The XRD patterns of the catalysts showed broad peaks around the 2θ value of 25.4° in common, originating from the disordered graphitic arrangement along the [002] direction (Fig. 1b). However, only Ni-SAC-900/H_2 among the catalysts exhibited two sharp peaks around the 2θ values of 44.4° and 51.8°, corresponding to the (111) and (200) peaks of metallic Ni particles. The presence of metallic Ni particles in only Ni-SAC-900/H_2 indicated that a severe carbonization process may not facilitate the accommodation of Ni atoms in a single atomic configuration but instead lead to their agglomeration into metallic Ni particles. This is also supported by HADDF-STEM observations (Fig. 1c, Fig. 1d, and Fig. S4). All Ni-SACs except Ni-SAC-900/H_2 exhibited isolated Ni features over N-doped carbon supports without any agglomeration on a certain spot. Furthermore, the elemental mapping results characterized the homogeneous Ni distribution. However, Ni nanoparticles ranging from 10 nm to 30 nm were obviously observed for Ni-SAC-900/H_2. Additionally, fluorescence signals corresponding to Ni were evident on the N-doped carbon surfaces, indicating the presence of Ni in both single-atomic configurations and agglomerated nanoparticles in Ni-SAC-900/H_2. On the other hand, Raman spectroscopy analyses (Fig. S5) were performed to examine the graphitization of the catalysts. All Ni-SACs exhibited distinct D-bands and G-bands. The G-band originates from sp^2-hybridized carbon domains, while the D-band arises from structural defects caused by interactions with elements such as Ni, N, and O or from sp^3-hybridization domain. The intensity ratio of the D-band to the G-band (I_D/I_G), commonly used as an indicator of the degree of graphitization, ranged from 0.98 to 0.99 across all samples, indicating a similar level of graphitization regardless of the carbonization conditions.

The XAFS analyses at Ni K-edge were performed to elucidate the local structure of Ni in a series of Ni-SACs (Fig. 2a and 2b). For comparison, those of Ni-Pc and Ni foil are included as the reference spectra representing the oxidation states of 2+ and 0+, respectively, in Fig. S6. As shown in Fig. 2a, all the Ni-SACs have similar characterized peaks in their XANES profiles. In comparison with those of Ni-Pc, there were only differences in their peak intensities and positions, suggesting Ni-SACs also have the planar square symmetry (D_{4h}) as in Ni-Pc. In the XANES results, the following points can be pointed out:

(1) The profiles for all Ni-SACs appear similar except for Ni-SAC-900/H_2. Unlike the other Ni-SACs, Ni-SAC-900/H_2 exhibits a relatively

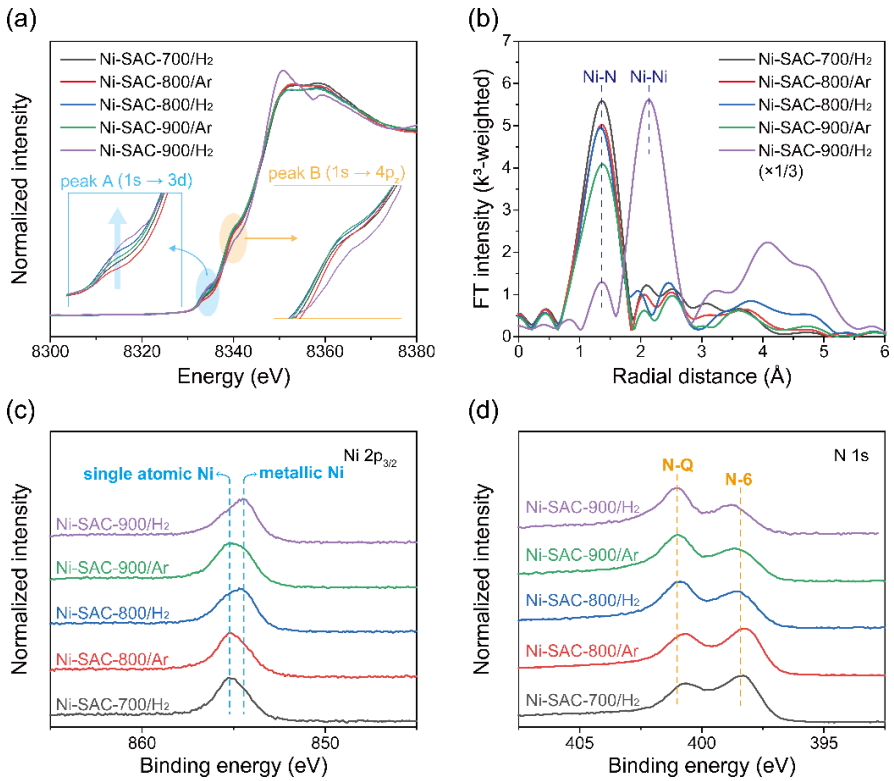

Fig. 2 Chemical structure analyses of Ni-SACs. (a) XANES and (b) EXAFS profiles at Ni K-edge. XPS spectra (c) in the Ni $2p_{3/2}$ branch and (d) in the N 1s branch.

sharp peak around 8334 eV, which can be attributed to the partial formation of Ni nanoparticles together with Ni single atomic sites.

(2) It is well-established that the intensity of the pre-edge (denoted as peak A), corresponding to the electronic transition of 1*s* → 3*d*, is proportional to the extent to which the centrosymmetric feature of the D_{4h} symmetry is distorted. In considering the negligible intensity of the pre-edge peak of Ni-Pc, the noticeable intensities of peak A in a series of Ni-SACs may represent the defective nature and/or locally elongated bonding in the Ni–N_x moieties.[23]

(3) The intensity of the electronic transition of 1*s* → 4p_z (denoted as peak B) around 8340 eV exhibits an opposite trend to that of peak A regarding the degree of distortion in the D_{4h} symmetry. While Ni-Pc showed a noticeable intensity of peak B, all the Ni-SACs exhibited a significant reduction in their peak B intensities, which is attributed again to the distortion in the D_{4h} symmetry.[23]

(4) The integrated areas for peak A (Fig. S7) and peak B (Fig. S8) were calculated to quantify the distortion degree of the D_{4h} symmetry in the catalysts, and the results are summarized in Fig. S9. Considering the integrated areas of peak A and peak B together with the degree of carbonization (Fig. 1a), it can be concluded that the reduction in the N content, as a result of the intensifying carbonization process, leads to the formation of Ni–N_x units in a nitrogen-deficient form, thereby accelerating the distortion of the D_{4h} symmetry.

To gain further insight into the coordination environment of Ni–N_x units in a series of Ni-SACs, we analyzed their EXAFS profiles (Fig. 2b). Because Ni-SACs are structurally inhomogeneous, containing various Ni–N_x configurations with different N coordination numbers, the fitting was performed by using Ni-Pc as a structural motif because it features individual Ni atoms isolated by four N atoms (*i.e.*, Ni–N_4) through covalent bonding (Fig. S10 and Tables S2–S8), which may offer insights into the local structure of the Ni–N_x units and the relative trends in N coordination of a series of Ni-SACs. The EXAFS fitting revealed that, except for Ni-SAC-900/H_2, the Ni atom in Ni-SACs was coordinated with 2.9−3.5 N atoms with a Ni–N bond length of ≈1.87 Å. This suggested that Ni may be coordinated not only by N but also by C or vacancies. It should be noticeable that the coordination number of the Ni–N for Ni-SAC-900/Ar was 2.9 ± 0.3.[49] As will be discussed in the following section, Ni-SAC-900/Ar exhibited the highest CO_2RR activity, which is in good agreement with recent theoretical predictions suggesting that the higher CO_2RR activity can be achieved when the N coordination is less than 4 with a proper amount of C and/or vacancies. In Ni-SAC-900/H_2, the Ni atom coordinated with 4.38 ± 0.05 Ni and 1.20 ± 0.07 N atoms, exhibiting features of both metallic Ni and single atomic Ni, respectively. This observation is also consistent with the HAADF-STEM and elemental mapping results in Fig. 1d. It is worth noting again that, as the degree of carbonization increases, the proportion of low N coordination sites becomes more dominant. In fact, the N coordination number is not strictly 1.20 ± 0.07 but rather reflects an average value representing the structural inhomogeneity of the Ni–N_x configurations in Ni-SAC-900/H_2.

Additionally, noteworthy findings from the ICP-OES and EA results indicate that increasing the heating temperature and using H_2 gas during the annealing process generally lead to an increase in Ni content with a significant reduction in the O and N contents (Table S1). Considering the XRD patterns (Fig. 1b) and EXAFS profiles

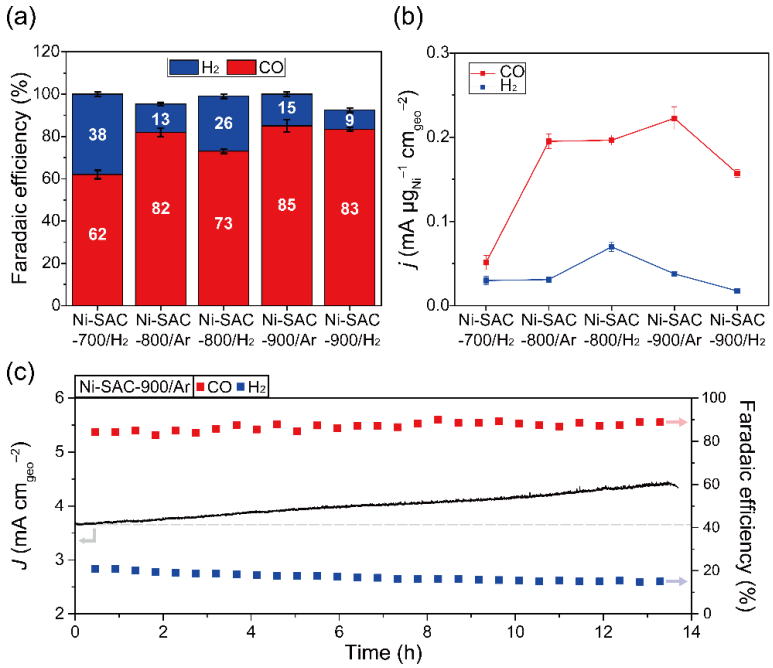

Fig. 3 Electrochemical evaluation for a series of Ni-SACs. (a) Faradaic efficiencies (%) and (b) partial current densities normalized by Ni contents (mA μg_{Ni}^{-1} cm_{geo}^{-2}) for CO and H_2 at –0.6 V_{RHE}. (c) Stability test of Ni-SAC-900/Ar performed at –0.6 V_{RHE}.

(Fig. S10e) associated with metallic Ni, which is only present in Ni-SAC-900/H_2, the formation of metallic Ni particles can be understood to occur when the N-doped carbon supports exceed the extent to which they can accommodate Ni in a single atomic configuration by covalent bonding with C and N atoms. This is also consistent with the high resolution Ni $2p_{3/2}$ results (Fig. 2c) that Ni-SAC-900/H_2 shows the XPS peak shift toward lower binding energies compared with other Ni-SACs.

High resolution XPS analyses were conducted to further confirm the chemical characteristics of N and Ni in a series of Ni-SACs. The high resolution N 1*s* data exhibited two major peaks around 398.7 eV and 401.0 eV, corresponding to the pyridine-like N-6 and graphite-like N-Q nitrogen configurations, respectively (Fig. 2d and Fig. S11).[23, 24, 50, 51] As increasing the C content in the catalysts, the N-6 portion relatively decreases while the N-Q portion increases, which might be attributed to the fact the N-doped carbon supports do not accommodate the N-6 configuration but the N-Q configuration in their defective graphitic array. Such a relationship is visualized more clearly in the correlation of the carbon content with N-6 and N-Q portions (Fig. S11f). The N-6 and N-Q contents for Ni-SACs were calculated by multiplying the N content obtained from the EA results (Table S1) by the fractions of N-6 and N-Q configurations derived from the XPS N1s spectra (Fig. S11a–e), respectively. The analysis reveals that, as the C content increases, both the N–6 and N–Q contents decrease, with a reduction in the fraction of N–6 and an increase in the fraction of N–Q.

3.2 Electrochemical performance

The CO_2RR activities of Ni-SACs were evaluated by using the CA technique in a high purity CO_2-saturated 0.5M $KHCO_3$ electrolyte in the gastight two-compartment H-type cell in the potential range from –0.4 V_{RHE} to –1.0 V_{RHE}. See the Experimental section for the detailed electrochemical conditions. The electrochemical CO_2RR performance of Ni-SACs is shown in Figs. S12–S19. All the catalysts exhibited CO and H_2 as the major products, with the sum of FE_{CO} and FE_{H2} being near 100%. As potentials increase negatively from –0.4 V_{RHE} to –1.0 V_{RHE}, FE_{CO} tends to increase, then saturate around –0.8 V_{RHE}, and finally decrease while FE_{H2} tends to decrease up to –0.8 V_{RHE} and afterward increase. This is attributed to the limited mass transport of CO_2 at high electrochemical potentials for the CO_2RR process, as evidenced by Tafel analyses (Fig. S20). The Tafel plots derived from the partial current densities (*i.e.*, J_{CO} and J_{H2}) indicate distinct Tafel slope regions in the potential range of –0.4 V_{RHE} to –0.6 V_{RHE}, suggesting that CO_2 transport limitations become significant beyond –0.6 V_{RHE}. Notably, Ni-SACs exhibit Tafel slope values ranging from 62 to 81 mV dec^{-1}, highlighting the efficiency of Ni–N_x sites in stabilizing adsorbed CO_2.[18] It is noteworthy that Ni-SAC-900/Ar, our optimal catalyst, retains its high FE_{CO} value (91%) in the range of –0.7 V_{RHE} to –1.0 V_{RHE}, confirming the robust Ni–N_x moiety as the catalytic active site for CO_2RR (Fig. S12).

It was found that their CO_2RR activity and selectivity toward CO production was appreciably affected by their Ni–N coordination environments originating from the synthetic conditions. When comparing FE_{CO} values of Ni-SACs at –0.6 V_{RHE} (Fig. 3a), Ni-SAC-900/Ar exhibited higher CO selectivity (85%) than the other Ni-SACs (62~83%), indicating the presence of optimal synthetic conditions capable of forming the most suitable Ni–N_x environment for CO evolution. With potentials being applied more negatively, partial current density based on the electrode area (J, mA cm_{geo}^{-2}, Fig. S13) increased as a result of the reaction rate. In comparing the J_{CO} values at –0.6 V_{RHE}, it was found that they have no significant correlation with the Ni contents (Table S1), which should be attributed to the

different chemical environments of Ni–N_x moieties. For example, even though Ni-SAC-800/Ar and Ni-SAC-700/H_2 have similar Ni contents (2.82 wt% vs. 2.93 wt%, respectively), Ni-SAC-800/Ar exhibited ~3.7 times higher J_{CO} value (2.2 ± 0.1 mA cm_{geo}^{-2}) than that of Ni-SAC-700/H_2 (0.6 ± 0.1 mA cm_{geo}^{-2}). Such a discrepancy between Ni content and J_{CO} values became more obvious when comparing Ni-SAC-900/Ar and Ni-SAC-800/H_2. Despite their similar Ni contents (3.71 wt% vs. 3.83 wt%, respectively), Ni-SAC-900/Ar showed higher J_{CO} (3.3 ± 0.2 mA cm_{geo}^{-2}) than Ni-SAC-800/H_2 (3.01 ± 0.09 mA cm_{geo}^{-2}).

To further understand the site-specific activity, we compared the areal current densities normalized by the Ni content (j, mA μg_{Ni}^{-1} cm_{geo}^{-2}) of the catalysts at –0.6 V_{RHE} (Fig. 3b). The comparison of j_{CO} values highlights the importance of both appropriate Ni loading and Ni–N coordination for favorable CO_2RR. Ni-SAC-900/H_2 exhibited a ~1.5 times higher J_{CO} value compared to Ni-SAC-800/Ar (3.4 ± 0.1 *vs.* 2.2 ± 0.1 mA cm_{geo}^{-2}). However, Ni-SAC-900/H_2 showed a lower j_{CO} value compared to Ni-SAC-800/Ar (0.49 ± 0.03 *vs.* 0.59 ± 0.07 mA μg_{Ni}^{-1} cm_{geo}^{-2}), indicating that the agglomerated Ni particles in Ni-SAC-900/H_2 (Fig. 1d), which could not be accommodated in a single atomic configuration and do not participate in the electrocatalytic CO_2-to-CO reaction. In this regard, the high CO_2RR activities of electrocatalysts featuring Ni nanoparticles on N-doped carbons[52-54] likely originate from the single atomic configuration of Ni embedded within the N-doped carbon supports.

Furthermore, in considering the coordination environment of Ni–N_x, the sample (Ni-SAC-900/Ar) with a lower N coordination (≈2.9 ± 0.3) to Ni showed the highest J_{CO} and j_{CO} values among the series of Ni-SACs. Thus, the atomically dispersed Ni sites with less than 4 N coordination appear to be optimal catalytic active sites for selective CO_2-to-CO conversion. This is further supported by the electrochemical results of Ni-SAC-900/H_2, which exhibited the lowest N coordination (1.20 ± 0.07). Despite the limited j_{CO} values originating from the substantial presence of metallic Ni nanoparticles, Ni-SAC-900/H_2 showed high J_{CO} values, indicating that the Ni–N_x units in nitrogen-deficient configurations played a critical role in promoting CO_2RR. On the other hand, Ni-SAC-700/H_2 showed the lowest J_{CO} and j_{CO} values. This might contradict the expectation that all the Ni atoms can be fully dispersed by sufficient N-6 to form a Ni–N_x complex with the highest x value (≈3.5 ± 0.2) that likely exhibits high CO_2RR activity. However, we believe that the coordination environments of Ni and N close to Ni–N_4 unit cannot provide structural flexibility during the interaction with CO_2RR intermediates, making the Ni–N_4 site less favorable for CO_2RR than the catalytic active sites with different N/C-containing ligand environments. This interpretation is also supported by the observed correlation between CO_2RR activity (*i.e.*, J_{CO}) and N coordination of Ni (x in the Ni–N_x unit), which demonstrates that CO_2RR activity consistently increases as the N coordination decreases (Fig. S21), which is further corroborated by our Tafel analyses (Fig. S20). Ni-SAC-700/H_2 exhibits a higher Tafel slope value (80.5 mV dec^{-1}) compared to other Ni-SACs (62.9~71.8 mV dec^{-1}). This finding indicates that, compared to the other Ni-SACs, which efficiently stabilize adsorbed CO_2 intermediates, the CO_2RR performance of Ni-SAC-700/H_2 is more likely limited by the first electron transfer step involved in the formation of a CO_2 intermediate (*i.e.*, * + CO_2 + e– → *CO_2^-).[18] The cathodic shift in the onset potential for the increase in cathodic current in the LSV curve for Ni-SAC-700/H_2 well aligns with this observation. And, the significantly larger R_{CT} value for Ni-SAC-700/H_2 (25.154 Ω cm^{-2}), which is 6.4~11.4 times higher than those of other Ni-SACs (2.203–3.919 Ω cm^{-2}), can also be understood in the same context (Fig. S22). The dependence of CO_2RR activity on the N coordination is supported by our *in-situ* XAFS results, as discussed in the following section, where the change in the degree of distortion in the D_{4h} symmetry is monitored upon applying electrochemical potentials. Previous reports also suggested that configurations such as Ni–N_3, Ni–N_2 and Ni–N_3C_1, which include vacancies and/or C atoms instead of N atoms, are more advantageous for CO_2RR than Ni–N_4 configuration.[24, 29, 30, 55, 56]

The long-term stability tests of a series of Ni-SACs were performed at –0.6 V_{RHE} (Fig. 3c and Fig. S23). It is important to note that, before stability tests, both catholyte and anolyte were purified using two graphite rods to remove any trace amount of metallic species, as suggested by Hori *et al*.[57] All the catalysts retained their original FE_{CO} and FE_{H2} values with negligible loss for 13 h. Ni-SAC-900/Ar showed a high FE_{CO} of ~90% with an average J of ~4.00 mA cm_{geo}^{-2}, outperforming the other catalysts in this work. In the stability test, Ni-SAC-700/H_2 exhibited a low J value and suffered from severe deactivation, which led to a significant loss of J after 13 h (0.48 → 0.09 mA cm_{geo}^{-2}), suggesting again the importance of the optimal Ni–N_x environment in the long-term stability of catalytic performance. The low stability of Ni-SAC-700/H_2 is likely attributed to its relatively high content of oxygen-containing functional groups (4.44 wt% O in Table S1), which are prone to be reduced during the CO_2RR process, thereby leading to catalyst degradation. Indeed, other Ni-SACs with oxygen contents exceeding 3% (*e.g.*, Ni-SAC-800/Ar and Ni-SAC-800/H_2) also exhibit activity degradation after 13 h, whereas Ni-SAC-900/Ar and Ni-SAC-900/H_2, with lower oxygen contents, maintain relatively stable catalytic performance (Fig. 3c and Fig. S23).

Ni-SAC-900/Ar (the best-performing catalyst) and Ni-SAC-700/H_2 (the worst-performing catalyst) were further evaluated in a GDE-based flow cell reactor[58] at –0.6 V_{RHE} for 10 h and the results were compared with those from the H-cell reactor (Figs. S24 and S25). Both catalysts exhibited stable current density profiles with significantly higher current densities in the flow cell compared to the H-cell. This enhancement is attributed to the direct delivery of gaseous CO_2 onto the catalyst layers in the flow cell, effectively eliminating the CO_2 transport limitations present in the H-cell setup, where dissolved CO_2 in electrolyte is used. Although both catalysts did not exhibit noticeable change in FE_{CO} values, their J values increased significantly due to the improved CO_2 supply. Ni-SAC-700/H_2 displayed a 2.3-fold increase in J values from 1.9 mA cm^{-2} to 4.3 mA cm^{-2} while Ni-SAC-900/Ar exhibited a 15-fold increase from 4.0 mA cm^{-2} to 59.8 mA cm^{-2}. The relatively low improvement in J for Ni-SAC-700/H_2 highlights again the intrinsic low activity of the Ni–N_4 sites for CO_2RR.

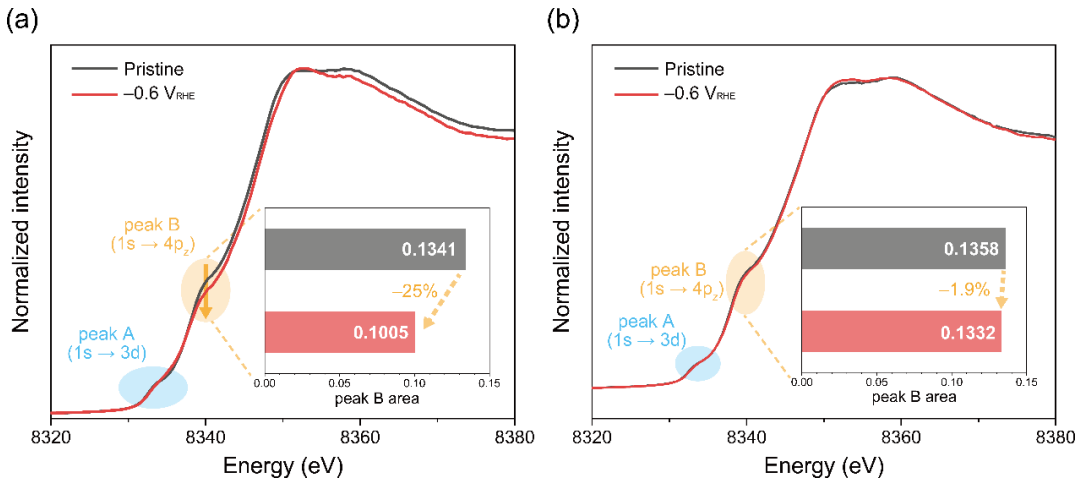

Fig. 4 *In-situ* XAFS results of (a) Ni-SAC-900/Ar and (b) Ni-SAC-700/H_2 at Ni K-edge.

3.3 *In-situ* XAFS analyses

In order to investigate the changes in the physicochemical structure of Ni–N_x moiety in a series of Ni-SACs during CO_2RR, we conducted *in-situ* XAFS analyses by using a 7-element Ge detector with a main focus on the XANES region at Ni K-edge (Fig. 4 and Fig. S26). The 7-element Ge detector allowed for selectively acquiring fluorescence signals originating from Ni during *in-situ* XAFS analysis. As a result, the local structural change of the single atomic Ni site upon the electrochemical potentials was effectively investigated. We first compared the XANES profiles of Ni-SAC-900/Ar at the pristine state and during CO_2RR at –0.6 V_{RHE} (Fig. 4a, Fig. S8d, and Fig. S27d). It was shown that, upon applying –0.6 V_{RHE}, the integrated area of peak B noticeably decreased by ~25.0% (0.1341 → 0.1005). Considering that the intensity of peak B increases as the D_{4h} symmetry is better maintained (*i.e.*, a larger area under peak B as more rigid D_{4h} symmetry), the decrease in the area of peak B at –0.6 V_{RHE} in the Ni-SAC-900/Ar catalyst compared with that at the pristine state indicates a further distortion of the planar square symmetry of Ni–N_x due to the interaction between Ni and CO_2RR intermediates. And, as aforementioned in 3.1 Section, peak B originates from the electronic transition from the filled 1s to the empty 4p_z states. Therefore, it can be understood that the decrease in peak intensity is attributed to the redistribution of electrons in Ni–N_x by the adsorption of CO_2RR intermediates to form a Ni–N–C bond.

We further investigated the XANES profile changes Ni-SAC-700/H_2, Ni-SAC-800/Ar, Ni-SAC-800/H_2, and Ni-SAC-900/H_2 (Fig. 4b, Fig. S26). Notably, the XANES profiles for Ni-SAC-700/H2 barely changed, with the integrated area of peak B nearly unchanged (0.1358 → 0.1332, –1.9%), indicating that the CO_2-intermediates could hardly interact with the Ni–N_x sites in Ni-SAC-700/H_2. This result is consistent with the lowest activity and selectivity of Ni-SAC-700/H_2 among the series of Ni-SACs (Figs. S12–S14). The changes in the integrated area of peak B followed a similar trend to the CO_2RR activity (Fig. S13and Fig. S28) in the order of Ni-SAC-900/H_2 (–29.1%) > Ni-SAC-900/Ar (–25%) > Ni-SAC-800/H_2 (–20.7%) > Ni-SAC-800/Ar (–9.2%) > Ni-SAC-700/H_2 (–1.9%), indicating that the interaction between CO_2 intermediates and Ni–N_x active sites has a significant impact on the CO_2RR activity of Ni-SACs. Considering the Ni–N coordination number of Ni-SAC-900/Ar (2.9 ± 0.3) and Ni-SAC-900/H_2 (1.20 ± 0.07) (Fig. S10, Tables S7 and S8), it can be concluded that an appropriate coordination of N/C to Ni on the Ni–N_x sites can enhance the CO_2RR by allowing for the favorable interaction with CO_2RR intermediates by a flexible distortion of Ni–N units during CO_2RR.

3.4 DFT calculations

To test the feasibility of our Ni-SAC models, we initiated our calculations to compute the formation energy (Fig. 5) and binding energy (Fig. S29) of various Ni–N_x configurations shown in Fig. S30 and Fig. S31, respectively. We have modeled two different single vacancies (SV1 and SV2), a double vacancy (DV), and a triple vacancy (TV). The SV1 and SV2 Ni-SACs with different Ni–N_x configurations are depicted in Fig. S30. Similarly, the DV- and TV-generated Ni–N_x moieties are depicted in Fig. S31. The SV models are produced by removing one carbon and replacing the site with Ni. The SV2 structures have 5-membered and 7-membered rings. DV and TV structures were created by removing two and three C atoms from the graphene plane and replaced by a Ni atom. In the case of SVs, the Ni protrudes out of the graphene plane during relaxation, losing planarity. However, Ni is accommodated perfectly in the graphene plane in the case of DV and TV, with a slight loss of planarity due to interacting Ni–N and Ni–C bonds. The formation energy, calculated following equation (1), is the primary criterion for finding a set of thermodynamically favorable Ni–N_x configurations on graphene, which represent the active sites of the Ni-SACs in our experimental measurements. We observed a decreasing trend in the formation energy as the number of N bonded to Ni increases. Formation energy for SV2 remains positive for all configurations, making structural rearrangement of single vacancy to form 5 and 7-membered rings highly unlikely. Formation of 3 C site vacancies on the graphene surface to accommodate Ni is also thermodynamically unfeasible, as observed from the positive formation energy. Owing to the size of the Ni, DV facilitates Ni atoms in the most stable configuration. For SV1 and DV, Ni substitution on the graphene surface with no N decoration has positive formation energy.

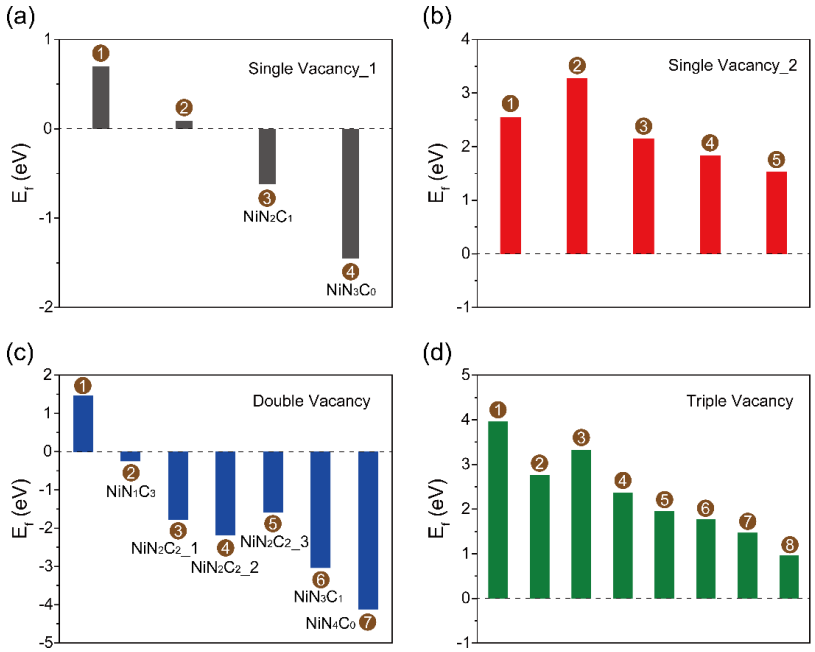

Fig. 5 DFT calculated formation energies of various Ni–N_x configurations in N-doped graphene layer. The number on the bar represents the type of Ni-SAC configurations shown in Fig. S30 and Fig. S31.

This suggests that N decoration stabilizes Ni substitution, leading to the formation of energetically favorable Ni–N_x configurations.[59, 60] Among all, DV has the most stable structures with the lowest formation energy. All six configurations with NiN_xC_y, (x = 1, 2, 3, and 4; y = 4–x) that have negative formation energy are considered for CO_2RR and HER. Two of the SV1s, termed NiN_2C_1-SV1 and NiN_3C_0-SV1, also have negative formation energy. Hence, these eight Ni–N_x configurations (NiN_2C_1_SV1, NiN_3C_0_SV1, NiN_1C_3_DV, NiN_2C_2-1_DV, NiN_2C_2-2_DV, NiN_2C_2-3_DV, NiN_3C_1_DV, NiN_4C_0_DV) are considered for reactivity analysis. Their DFT-optimized bond length for the Ni center and its first neighboring atoms (*i.e.*, Ni–N and Ni–C) are tabulated in Table S9. For the Ni–N_4C_0_DV configuration, all Ni–N bond lengths are equal at 1.88 Å, which maintains a high degree of D_{4h} symmetry. However, as C atoms replace N atoms, the symmetry becomes progressively distorted. For example, for the Ni-N_2C_2-1_DV configuration, the Ni–C bond lengths are consistently shorter at 1.83 Å, while the Ni–N bond lengths are elongated to 1.94 Å and 1.95 Å, respectively. These results demonstrate that a decrease in N coordination systematically disrupts the D_{4h} symmetry of the Ni–N_x active sites, a trend that correlates well with the reduction in the integrated area of peak B observed in the EXAFS spectra as the fitted N coordination number decreases (Fig. S8 and Tables S3–S8). The binding energies of Ni single atom to the graphene surface are all negative (Fig. S29). The binding energy provides an equitable description of the stability of Ni–N_x graphene catalysts. We have also compared the stability of Ni–N_x sites to the cohesive energy of Ni, *i.e.*, –5.97 eV. All the DV structures have stronger Ni binding compared to metallic Ni bulk, which further highlights the feasibility and stability of DV-supported Ni–N_x sites, namely, NiN_1C_3_DV, NiN_2C_2_DV, NiN_3C_1_DV, and NiN_4C_0_DV.

The CO_2RR catalyzed by Ni-SACs is investigated following reactions (R1), (R2), and (R3). The CO_2RR to CO is a 2 electron-transfer reaction. Our calculations show that CO_2RR preferentially takes place on the Ni site. The first step of CO_2RR is the simultaneous adsorption and protonation of CO_2 to form *COOH, followed by its reduction to *CO + H_2O(g) and the non-electrochemical desorption process of the molecular CO(g). The optimized structures of *COOH and *CO on different Ni-SACs are presented in Fig. S32. The free energy barriers, calculated at pH = 7, for CO_2RR catalyzed by eight different Ni–N_x sites are plotted in Fig. 6a. The free energy barrier of *COOH formation is the potential determining step (PDS) for DV and CO(g) desorption is the PDS for the SV-based Ni–N_x sites. For DV-related Ni–N_x sites, an increase in the reaction barrier is observed with increasing N coordination with Ni. From Bader charge analysis (Table S10), we observed that with increasing N count, the Ni becomes partially positively charged and increasingly electrophilic.[61, 62] Thus, CO_2 adsorption and reduction become more energy-demanding as the N coordination around Ni increases. Irrespective of the vacancy type, the *CO formation from *COOH is a thermodynamically favorable process and downhill energetically. The CO(g) desorption plays a significant role in determining the catalytic efficiency, and in particular, the strong CO binding leads to CO poisoning. Hence, the catalyst that has moderation between COOH adsorption and molecular CO desorption is considered a better candidate for CO_2RR. On both SV1-based Ni–N_x sites, *COOH formation is associated with a low free energy change (Fig. 6a) compared to DV-based Ni–N_x sites. However, *CO posing is evident in the SV1-based Ni–N_x sites.

The DFT predicted limiting potentials for CO_2RR on all Ni–N_x sites, which were calculated following equation (9), are given in Table S11. From a theoretical perspective, we observed that NiN_4C_0_DV is an

ineffective catalyst due to a reaction barrier of 1.81 eV for *COOH formation. Also, we rule out the SV1-based Ni–N_x sites as active sites owing to CO poisoning based on their strong CO binding energies leading to high barriers for *CO desorption (0.65 eV and 0.96 eV on NiN_2C_1_SV1 and NiN_3C_0_SV1, respectively). After elimination, we are left with NiN_1C_3_DV, NiN_2C_2-1_DV, NiN_2C_2-2_DV, NiN_2C_2-3_DV, and NiN_3C_1_DV. Thus, the DFT calculations predict that Ni–N_x (x= 2–3) sites show moderate free energy change for all steps of CO_2RR, which is consistent with the average N coordination number of 2.9 ± 0.3 for the most effective catalyst observed in our experiments (Fig. 3).

During an electrochemical process, the transfer of electrons and intermediate adsorption changes the local structure of the reactive surface. As *COOH and *CO adsorb on the surface, the Ni–N and Ni–C bond lengths increase. The bond length and dihedral angle before and after intermediate adsorption are tabulated in Table S12. For NiN_2C_2-1_DV, the Ni–N bond length increases from 1.94 Å to 1.96 Å and 1.99 Å after *COOH and *CO adsorption, respectively. Similarly, *COOH and *CO formation on NiN_2C_2-3_DV alters the Ni–N bond length from 1.89 Å to 1.92 Å and 1.96 Å, respectively. Ni atom also protrudes out of the surface, losing planarity of the DV surface, as observed by the change in dihedral angle. Such a change in the bond length and dihedral angle is associated with the weakening D_{4h} symmetry of the Ni–N_x unit upon the intermediate adsorption, which is also consistent with *in-situ* XANES results (Fig. 4).

We have plotted the correlation between *COOH adsorption energy (G_{ads}(COOH)) and ΔG_{PDS} and the correlation between *CO adsorption energy (G_{ads}(CO)) and ΔG_{PDS} for the series of DV-based Ni-SACs in Fig. S33.[63, 64] We have excluded the SV-based Ni-SACs due to the aforementioned CO poisoning. We observed a linear relationship among G_{ads}(COOH) and ΔG_{PDS}, with G_{ads}(COOH) aligning perfectly in a line (R^2 = 0.99). However, G_{ads}(CO) values do not align perfectly, deteriorating the correlation coefficient (R^2 = 0.93).

The near-perfect linear correlation among G_{ads}(COOH) and ΔG_{PDS} suggests that the PDS depends on the first step of CO_2RR, *i.e.*, COOH adsorption energy rather than the *CO desorption step. Thus, G_{ads}(COOH) is identified as a descriptor for CO_2RR catalyzed by Ni–N_x sites, and likely by TM–N_x (TM = transition metals) sites, embedded in a graphene plane in line with the results from previous DFT study of CO_2RR on SACs.[65] More importantly, this descriptor can be easily calculated using simple DFT binding energy calculations, which help identify potential TM-N_x configurations that show favorable selectivity of CO_2RR to CO. Therefore, the identification of such a simple catalytic descriptor is significant for the accelerated design and development of CO_2RR catalysts composed of TM-N_x configurations.

During reduction reactions, there is a likelihood of the reactive proton getting adsorbed on the active site, hindering the interaction of CO_2RR reactive species. As the elementary steps of CO_2RR involve proton-coupled electron transfer, the proton adsorption on the Ni site is unavoidable. Thus, a catalyst whose active site prefers CO_2 adsorption rather than proton adsorption is conceived as a promoter of CO_2RR. So, a good catalyst for CO_2RR should have a moderate binding affinity for *COOH, *CO, and weak interaction with *H. Thus, we have calculated the free energy of *H formation on Ni–N_x sites, and the results are plotted in Fig. 6b. The optimized structures of *H on different Ni-SACs are presented in Fig. S34. On the Ni–N_x sites studied here, either the *COOH or *CO formation is the PDS of CO_2RR. For HER, the NiN_1C_3_DV has a positive barrier for *H desorption, and for the rest, the *H formation is energetically demanding. HER reaction barrier values for the most energy-demanding step are given in Table S11. Our analysis shows that the Ni–N_x sites having positive ΔU_{PDS} or negative ΔU_{PDS} values close to zero prefer the CO_2RR over HER. The difference between the limiting potentials for CO_2RR and HER (ΔU_{PDS}) is predicted to be a descriptor of CO_2RR on Ni–N_x sites (Table S11).[33, 65] The ΔU_{PDS} values, plotted in Fig. 7, suggest four Ni–N_x sites models, namely, NiN_2C_1_SV1, NiN_2C_2-1_DV, NiN_2C_2-3_DV, and NiN_4C_0_DV, readily promote the CO_2RR compared to HER. However, we eliminated NiN_2C_1_SV1 as it suffers from CO poisoning, being associated with a high *CO desorption barrier of 0.65 eV, and NiN_4C_0_DV due to the markedly high energy barrier of 1.81 eV for *COOH formation. It is also noteworthy that Ni-SAC-700/H_2, which has the highest N coordination number of 3.5 ± 0.2, has the lowest total current densities among the series of Ni-SACs. It can be understood as a result of high energy barriers for both *COOH (1.81 eV) and *H (2.07 eV) formation on the NiN_4C_0_DV rich Ni-SAC-700/H_2, leading to unfavorable thermodynamics for CO_2RR and HER. To this end, we find two plausible candidates, NiN_2C_2-1_DV and NiN_2C_2-3_DV, as the best Ni–N_x sites for selectively promoting the CO_2RR. Three different NiN_2C_2_DV SACs are studied with identical N coordination for CO_2RR and HER. A difference in the adsorption energetics of key intermediates of CO_2RR and HER was observed on Ni–N_x configurations with the same N coordination. The density of states (DOS), d-band center (ε_d), and charge density distribution (CDD) around Ni and N in Ni–N_x configurations were computed to pinpoint the origin of the difference in selectivity of Ni–N_x configurations with the same number of N coordination (Fig. S35 and Table S13). The PDOS and ε_d are plotted and correlated with the *COOH and *H formation energy. For NiN_2C_2-2_DV the ε_d is closer to the Fermi level at –0.91 eV compared to NiN_2C_2-1_DV and NiN_2C_2-3_DV for which ε_d lies at –1.01 and –1.03 eV. The ΔG values for *COOH formation are 1.13, 1.18, and 1.05 eV, and those for *H formation are 1.06, 0.69, and 1.24 eV on NiN_2C_2-1_DV, NiN_2C_2-2_DV, and NiN_2C_2-3_DV, respectively. We observed that ε_d shift significantly affects the *H adsorption, however, *COOH adsorption is mildly affected. An upward shift of ε_d towards the Fermi level leads to stronger bonding of reaction intermediates, which reduces the free energy change for effective adsorption. A low-lying ε_d of NiN_2C_2-1_DV and NiN_2C_2-3_DV do not adsorb ($H^+ + e^-$) effectively and leave the site vacant for CO_2RR intermediates. Similar effects of ε_d on the H adsorption have been observed for Ru nanoparticles[66] and CoN_4 single-atom catalysts.[67] This DFT prediction of low N coordinated Ni sites as active sites of CO_2RR is consistent with our experimental observation of an increase in CO_2RR catalytic activity with decreasing N coordination of Ni on Ni–N_x units.

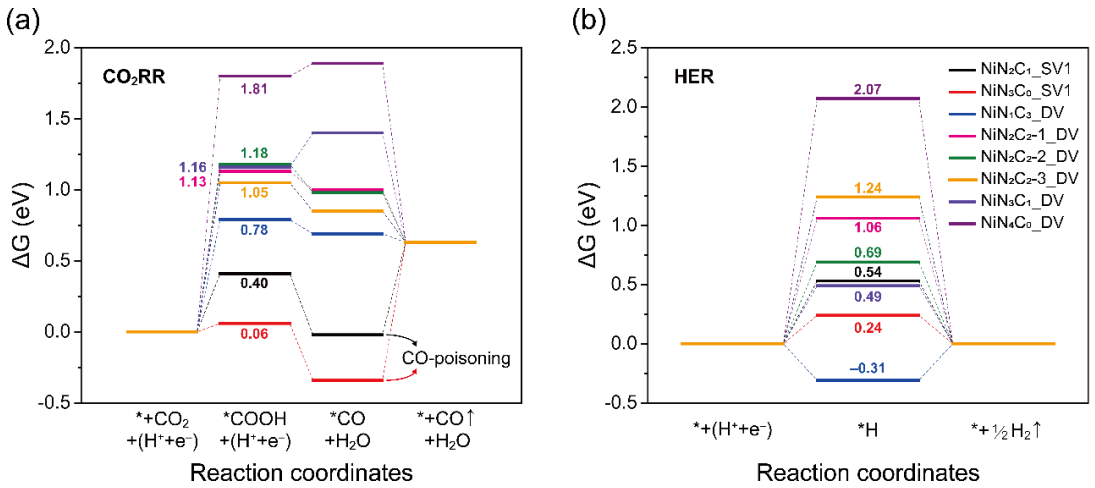

Fig. 6 Free energy diagram for (a) CO_2RR and (b) HER catalyzed by eight Ni-SAC models with negative formation energy values in a water solvent. The pH effect is included implicitly at pH = 7 and potential (U) = 0 V_{RHE}.

The effect of external potential on the free energy change of the CO_2RR and HER elementary steps is plotted in Fig. S36. The calculations are performed following the equation, $\Delta G_U = \Delta G_o + eU_{RHE}$, where U_{RHE} = the applied potential vs RHE, ΔG_o = free energy change calculated at pH = 7 (0.5M $KHCO_3$ electrolyte), ΔG_U = free energy change after application of U_{RHE} at pH = 7. For NiN_2C_1_SV1 and NiN_3C_0_SV1, it was observed that *CO desorption becomes the potential determining step at a very low reductive potential of 0.12 V and 0.74 V. Hence, at pH = 7, the possibility of CO poisoning prevails throughout the CO_2RR and HER potential range. With applied potential, the free energy change for *COOH and H* formation step lowers in value but *CO desorption remains as a highly endothermic step. For NiN_1C_1_DV, NiN_2C_2-1_DV, NiN_2C_2-2_DV, NiN_2C_2-3_DV, NiN_3C_1_DV, and NiN_4C_0_DV the *CO desorption step becomes PDS beyond U_{RHE} = –0.86, –1.51, –1.55, –1.46, –1.94 and –3.34 V, respectively. We eliminated NiN_1C_1_DV as for *CO desorption becomes PDS after –0.86 V, which is within our experimentally studied CO_2RR potential range of –0.4 to –1.0 V. Rest of the DV structures show *CO poisoning at a potential range of –1.46 to –3.34 V, higher than our experimental potential range of CO_2RR. Further screening of Ni-SAC is performed based on free energy change of electrochemical steps of CO_2RR and HER. As the criteria for a better catalyst, HER PDS must have a higher positive free energy change compared to the *COOH formation step, or the difference between the two must be very low. The DV Ni-SACs that satisfy the criteria in the experimental ranges of U values are NiN_2C_2-1_DV, NiN_2C_2-3_DV, and NiN_4C_0_DV. Compared to NiN_2C_2_DV SACs, NiN_4C_0_DV has a highly endothermic *COOH formation throughout the CO_2RR potential range. The potential dependent ΔG_U shows that NiN_2C_2-1_DV and NiN_2C_2-3_DV models concur with our experimental results.

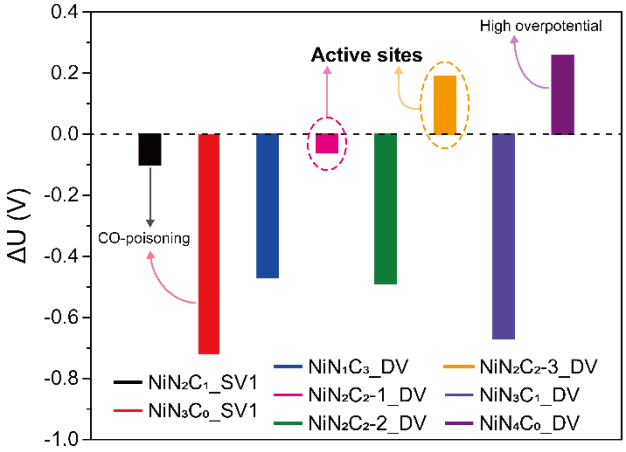

Fig. 7 ΔU_{PDS} values on eight Ni-SAC models.

4 Conclusions

A combination of experimental measurements and DFT calculations were performed to understand the structure-activity/selectivity relationships of Ni-SACs for the electrochemical CO_2RR process. The results show that the N-ligand environment of Ni atomic sites plays a significant role in steering the CO_2RR activity/selectivity of Ni-SACs. Experimentally, EXAFS fitting of the best performing Ni-SAC (*i.e.*, Ni-SAC-900/Ar) reveals that an N coordination number of 2.9 ± 0.3 to Ni is optimal for the selective CO_2RR over HER. This suggests that the Ni-SACs, where the Ni atom is coordinated with both N and C atoms to form the Ni–N_x sites with less than 4 N coordination (*i.e.*, Ni–N_x sites, x < 4), act as a better catalyst for CO_2RR compared to Ni-SACs with Ni–N_4 sites. Experimental results also provide insights into the local structural evolution of Ni in the Ni-SACs, highlighting the interplay among carbonization, N coordination, and Ni nanoparticle formation. As the degree of carbonization increases, the N content decreases, limiting the ability to stabilize Ni in single atomic configurations and leading to the formation of Ni nanoparticles through agglomeration. The experimental results were corroborated by the DFT prediction of selective CO_2RR on NiN_2C_2-1_DV and NiN_2C_2-3_DV sites. *In-si*

tu XAFS characterization of Ni-SAC-900/Ar reveals a loss of square pl anar D_{4h} symmetry of the catalyst surface, which is further supporte d by the DFT calculated elongation of Ni–N bond length and loss of planarity of Ni–N_x sites upon the adsorption of reaction intermediat es. The DFT calculated difference of limiting potentials for CO_2RR an d HER (ΔU_{PDS}) correlates well with the experimentally observed CO_2 RR activity and is predicted to be a descriptor of CO_2RR on Ni-SACs with built-in Ni–N_x active sites. Finally, our study provides a compre hensive guiding principle for the bottom-up design of Ni-SACs for se lective CO production from CO_2RR.

Data availability

The data supporting this article have been included as part of the Supplementary Information.

Author contributions

Min Sung Kim: Formal analysis, Conceptualization, Investigation, Methodology, Validation, Visualization, Writing – original draft, Writing – review & editing. Adyasa Priyadarsini: Formal analysis, Investigation, Methodology, Validation, Visualization, Writing – original draft, Writing – review & editing. Ju-Hyeon Lee: Formal analysis, Validation, Investigation. Jin-Gyu Bae: Formal analysis, Validation, Investigation. Jeong Yeon Heo: Formal analysis, Validation, Investigation. Hyeon Jeong Lee: Conceptualization, Funding acquisition, Project administration, Resources, Supervision, Writing – original draft, Writing – review & editing. Shyam Kattel: Conceptualization, Funding acquisition, Project administration, Resources, Supervision, Writing – original draft, Writing – review & editing. Ji Hoon Lee: Conceptualization, Funding acquisition, Project administration, Resources, Supervision, Writing – original draft, Writing – review & editing.

Conflicts of interest

The authors declare that they have no known competing financial interests or personal relationships that could have appeared to influence the work reported in this paper.

Acknowledgements

This research was supported by the National Research Foundation of Korea funded by the Ministry of Science and ICT (NRF-2022R1C1C1004171 and RS-2024-00345331). This work used Expanse at the University of California San Diego through allocation CHM240007 and CHE200036 from the Advanced Cyberinfrastructure Coordination Ecosystem: Services & Support (ACCESS) program, which is supported by National Science Foundation grants #2138259, #2138286, #2138307, #2137603, and #2138296. This research used resources of the National Energy Research Scientific Computing Center, a DOE Office of Science User Facility supported by the Office of Science of the U.S. Department of Energy under Contract No. DE-AC02-05CH11231 using NERSC award BES-ERCAP0027318 and Theory and Computation facility of the Center for Functional Nanomaterials (CFN), which is a U.S. Department of Energy Office of Science User Facility, at Brookhaven National Laboratory under Contract No. DE-SC0012704.The authors also acknowledge technical supports with 7D, 8C, and 10C beamlines of the Pohang Light Source-II in the Pohang Accelerating Laboratory.

References

1. Y. Wang, J. Mao, X. Meng, L. Yu, D. Deng and X. Bao, *Chem. Rev.*, 2019, **119**, 1806-1854.
2. Q. Zhang and J. Guan, *Adv. Funct. Mater.*, 2020, **30**, 2000768.
3. J. Zhang, W. Cai, F. X. Hu, H. Yang and B. Liu, *Chem. Sci.*, 2021, **12**, 6800-6819.
4. Q. Chang, Y. Liu, J.-H. Lee, D. Ologunagba, S. Hwang, Z. Xie, S. Kattel, J. H. Lee and J. G. Chen, *J. Am. Chem. Soc.*, 2022, **144**, 16131-16138.
5. J. Guan, Z. Duan, F. Zhang, S. D. Kelly, R. Si, M. Dupuis, Q. Huang, J. Q. Chen, C. Tang and C. Li, *Nat. Catal.*, 2018, **1**, 870-877.
6. J. Feng, H. Gao, L. Zheng, Z. Chen, S. Zeng, C. Jiang, H. Dong, L. Liu, S. Zhang and X. Zhang, *Nat. Commun.*, 2020, **11**, 4341.
7. Y. Pan, S. Liu, K. Sun, X. Chen, B. Wang, K. Wu, X. Cao, W.-C. Cheong, R. Shen, A. Han, Z. Chen, L. Zheng, J. Luo, Y. Lin, Y. Liu, D. Wang, Q. Peng, Q. Zhang, C. Chen and Y. Li, *Angew. Chem.-Int. Edit.*, 2018, **57**, 8614-8618.
8. T. N. Huan, N. Ranjbar, G. Rousse, M. Sougrati, A. Zitolo, V. Mougel, F. Jaouen and M. Fontecave, *ACS Catal.*, 2017, **7**, 1520-1525.
9. X. X. Wang, D. A. Cullen, Y.-T. Pan, S. Hwang, M. Wang, Z. Feng, J. Wang, M. H. Engelhard, H. Zhang, Y. He, Y. Shao, D. Su, K. L. More, J. S. Spendelow and G. Wu, *Adv. Mater.*, 2018, **30**, 1706758.
10. Y. Wu, Z. Jiang, X. Lu, Y. Liang and H. Wang, *Nature*, 2019, **575**, 639-642.
11. H. Fei, J. Dong, Y. Feng, C. S. Allen, C. Wan, B. Volosskiy, M. Li, Z. Zhao, Y. Wang, H. Sun, P. An, W. Chen, Z. Guo, C. Lee, D. Chen, I. Shakir, M. Liu, T. Hu, Y. Li, A. I. Kirkland, X. Duan and Y. Huang, *Nat. Catal.*, 2018, **1**, 63-72.
12. H.-J. Qiu, Y. Ito, W. Cong, Y. Tan, P. Liu, A. Hirata, T. Fujita, Z. Tang and M. Chen, *Angew. Chem.-Int. Edit.*, 2015, **54**, 14031-14035.
13. Y. Qu, Z. Li, W. Chen, Y. Lin, T. Yuan, Z. Yang, C. Zhao, J. Wang, C. Zhao, X. Wang, F. Zhou, Z. Zhuang, Y. Wu and Y. Li, *Nat. Catal.*, 2018, **1**, 781-786.
14. H. Wu, H. Li, X. Zhao, Q. Liu, J. Wang, J. Xiao, S. Xie, R. Si, F. Yang, S. Miao, X. Guo, G. Wang and X. Bao, *Energy Environ. Sci.*, 2016, **9**, 3736-3745.
15. S. Back, A. R. Kulkarni and S. Siahrostami, *ChemCatChem*, 2018, **10**, 3034-3039.
16. H. Niu, X. Wan, X. Wang, C. Shao, J. Robertson, Z. Zhang and Y. Guo, *ACS Sustain. Chem. Eng.*, 2021, **9**, 3590-3599.
17. R. Kottayintavida and N. K. Gopalan, *Int. J. Hydrog. Energy*, 2020, **45**, 8396-8404.
18. Q. He, J. H. Lee, D. Liu, Y. Liu, Z. Lin, Z. Xie, S. Hwang, S. Kattel, L. Song and J. G. Chen, *Adv. Funct. Mater.*, 2020, **30**, 2000407.
19. J. Yin, J. Jin, M. Lu, B. Huang, H. Zhang, Y. Peng, P. Xi and C.-H. Yan, *J. Am. Chem. Soc.*, 2020, **142**, 18378-18386.

20. M. Xiao, J. Zhu, G. Li, N. Li, S. Li, Z. P. Cano, L. Ma, P. Cui, P. Xu, G. Jiang, H. Jin, S. Wang, T. Wu, J. Lu, A. Yu, D. Su and Z. Chen, *Angew. Chem.-Int. Edit.*, 2019, **58**, 9640-9645.
21. K. Jiang, B. Liu, M. Luo, S. Ning, M. Peng, Y. Zhao, Y.-R. Lu, T.-S. Chan, F. M. F. de Groot and Y. Tan, *Nat. Commun.*, 2019, **10**, 1743.
22. R. Kamai, K. Kamiya, K. Hashimoto and S. Nakanishi, *Angew. Chem.*, 2016, **128**, 13378-13382.
23. H. B. Yang, S.-F. Hung, S. Liu, K. Yuan, S. Miao, L. Zhang, X. Huang, H.-Y. Wang, W. Cai, R. Chen, J. Gao, X. Yang, W. Chen, Y. Huang, H. M. Chen, C. M. Li, T. Zhang and B. Liu, *Nat. Energy*, 2018, **3**, 140-147.
24. Y. Zhou, Q. Zhou, H. Liu, W. Xu, Z. Wang, S. Qiao, H. Ding, D. Chen, J. Zhu, Z. Qi, X. Wu, Q. He and L. Song, *Nat. Commun.*, 2023, **14**, 3776.
25. S. Liu, H. B. Yang, S.-F. Hung, J. Ding, W. Cai, L. Liu, J. Gao, X. Li, X. Ren, Z. Kuang, Y. Huang, T. Zhang and B. Liu, *Angew. Chem.-Int. Edit.*, 2020, **59**, 798-803.
26. I. Song, Y. Eom, M. A. P, D. H. Hong, M. Balamurugan, R. Boppella, D. H. Kim and T. K. Kim, *Small*, 2023, **19**, 2300049.
27. M. D. Hossain, Y. Huang, T. H. Yu, W. A. Goddard Iii and Z. Luo, *Nat. Commun.*, 2020, **11**, 2256.
28. H. Han, J. Im, M. Lee and D. Choo, *Appl. Catal. B-Environ.*, 2023, **320**, 121953.
29. Y. Zhang, L. Jiao, W. Yang, C. Xie and H.-L. Jiang, *Angew. Chem.-Int. Edit.*, 2021, **60**, 7607-7611.
30. C. Yan, H. Li, Y. Ye, H. Wu, F. Cai, R. Si, J. Xiao, S. Miao, S. Xie, F. Yang, Y. Li, G. Wang and X. Bao, *Energy Environ. Sci.*, 2018, **11**, 1204-1210.
31. S. Brunauer, P. H. Emmett and E. Teller, *J. Am. Chem. Soc.*, 1938, **60**, 309-319.
32. B. C. Lippens and J. H. de Boer, *J. Catal.*, 1965, **4**, 319-323.
33. J. H. Lee, S. Kattel, Z. Jiang, Z. Xie, S. Yao, B. M. Tackett, W. Xu, N. S. Marinkovic and J. G. Chen, *Nat. Commun.*, 2019, **10**, 3724.
34. M. K. Kim, B. Lamichhane, B. Song, S. Kwon, B. Wang, S. Kattel, J. H. Lee and H. M. Jeong, *Appl. Catal. B-Environ. Energy*, 2024, **352**, 124037.
35. M. S. Kim, B. Lamichhane, J.-H. Lee, J.-G. Bae, J. Y. Heo, H. J. Lee, S. Kattel and J. H. Lee, *J. Energy Chem.*, 2023, **87**, 89-97.
36. G. Kresse and J. Furthmüller, *Phys. Rev. B*, 1996, **54**, 11169-11186.
37. P. E. Blöchl, *Phys. Rev. B*, 1994, **50**, 17953-17979.
38. J. P. Perdew, K. Burke and M. Ernzerhof, *Phys. Rev. Lett.*, 1996, **77**, 3865-3868.
39. S. Grimme, *J. Comput. Chem.*, 2004, **25**, 1463-1473.
40. S. Grimme, *J. Comput. Chem.*, 2006, **27**, 1787-1799.
41. K. Mathew, R. Sundararaman, K. Letchworth-Weaver, T. A. Arias and R. G. Hennig, *J. Chem. Phys.*, 2014, **140**.
42. J. Rossmeisl, A. Logadottir and J. K. Nørskov, *Chem. Phys.*, 2005, **319**, 178-184.
43. J. Rossmeisl, Z. W. Qu, H. Zhu, G. J. Kroes and J. K. Nørskov, *J. Electroanal. Chem.*, 2007, **607**, 83-89.
44. A. A. Peterson, F. Abild-Pedersen, F. Studt, J. Rossmeisl and J. K. Nørskov, *Energy Environ. Sci.*, 2010, **3**, 1311-1315.
45. J. K. Nørskov, T. Bligaard, A. Logadottir, J. R. Kitchin, J. G. Chen, S. Pandelov and U. Stimming, *J. Electrochem. Soc.*, 2005, **152**, J23.
46. Q. Liang, G. Brocks and A. Bieberle-Hütter, *J. Phys-Energy*, 2021, **3**, 026001.
47. G. Yang, H. Han, T. Li and C. Du, *Carbon*, 2012, **50**, 3753-3765.
48. K. Y. Kang, B. I. Lee and J. S. Lee, *Carbon*, 2009, **47**, 1171-1180.
49. X. Wang, Z. Chen, X. Zhao, T. Yao, W. Chen, R. You, C. Zhao, G. Wu, J. Wang and W. Huang, *Angew. Chem.*, 2018, **130**, 1962-1966.
50. H. M. Jeong, J. W. Lee, W. H. Shin, Y. J. Choi, H. J. Shin, J. K. Kang and J. W. Choi, *Nano Lett.*, 2011, **11**, 2472-2477.
51. J. H. Lee, N. Park, B. G. Kim, D. S. Jung, K. Im, J. Hur and J. W. Choi, *ACS Nano*, 2013, **7**, 9366-9374.
52. T. Yue, Y. Chang, J. Liu, J. Jia and M. Jia, *ChemElectroChem*, 2021, **8**, 4233-4239.
53. J. Jia, H. Yang, G. Wang, P. Huang, P. Cai and Z. Wen, *ChemElectroChem*, 2018, **5**, 471-477.
54. Z. Zhu, Z. Li, X. Wei, J. Wang, S. Xiao, R. Li, R. Wu and J. S. Chen, *Carbon*, 2021, **185**, 9-16.
55. X. Rong, H. J. Wang, X. L. Lu, R. Si and T. B. Lu, *Angew. Chem.*, 2020, **132**, 1977-1981.
56. K. Mou, Z. Chen, X. Zhang, M. Jiao, X. Zhang, X. Ge, W. Zhang and L. Liu, *Small*, 2019, **15**, 1903668.
57. Y. Hori, H. Konishi, T. Futamura, A. Murata, O. Koga, H. Sakurai and K. Oguma, *Electrochim. Acta*, 2005, **50**, 5354-5369.
58. K. Liu, W. A. Smith and T. Burdyny, *ACS Energy Lett.*, 2019, **4**, 639-643.
59. Y. Wang, L. You and K. Zhou, *Chem. Sci.*, 2021, **12**, 14065-14073.
60. A. D. Nishchakova, D. A. Bulushev, S. V. Trubina, O. A. Stonkus, Y. V. Shubin, I. P. Asanov, V. V. Kriventsov, A. V. Okotrub and L. G. Bulusheva, *Nanomaterials*, 2023, **13**, 545.
61. S. Back, J. Lim, N.-Y. Kim, Y.-H. Kim and Y. Jung, *Chem. Sci.*, 2017, **8**, 1090-1096.
62. S. Wang, B. Cheng, X. Fang, M. Cao, X. Xu and X. Wang, *J. Mol. Model.*, 2024, **30**, 138.
63. H. Cabrera-Tinoco, L. Borja-Castro, R. Valencia-Bedregal, A. Perez-Carreño, A. Lalupu-García, I. Veliz-Quiñones, A. G. Bustamante Dominguez, C. H. W. Barnes and L. De Los Santos Valladares, *Langmuir*, 2024, **40**, 6703-6717.
64. Y. Tang, W. Chen, C. Li, W. Li and X. Dai, *J. Phys.-Condes. Matter*, 2015, **27**, 255009.
65. B. An, J. Zhou, Z. Zhu, Y. Li, L. Wang and J. Zhang, *Fuel*, 2022, **310**, 122472.
66. Q. Hu, K. Gao, X. Wang, H. Zheng, J. Cao, L. Mi, Q. Huo, H. Yang, J. Liu and C. He, *Nat. Commun.*, 2022, **13**, 3958.
67. B. Cao, M. Hu, Y. Cheng, P. Jing, B. Liu, B. Zhou, X. Wang, R. Gao, X. Sun, Y. Du and J. Zhang, *NPG Asia Mater.*, 2021, **13**, 1.

Journal of Materials Chemistry A Paper

Ligand Environment Engineering of Nickel Single Atomic Sites for Efficient Electrochemical Carbon Dioxide Reduction Reaction

Received 00th January 20xx,
Accepted 00th January 20xx

DOI: 10.1039/x0xx00000x

Min Sung Kim,‡[ab] Adyasa Priyadarsini,‡[c] Ju-Hyeon Lee,[ab] Jin-Gyu Bae,[ab] Jeong Yeon Heo,[ab] Hyeon Jeong Lee,[d] Shyam Kattel,*[e] and Ji Hoon Lee,*[ab]*

Data availability

The data supporting this article have been included as part of the Supplementary Information.

[a.] *School of Materials Science and Engineering, Kyungpook National University, Daegu 41566, Republic of Korea. E-mail: jihoonlee@knu.ac.kr*
[b.] *KNU Advanced Material Research Institute, Kyungpook National University, Daegu 41566, Republic of Korea*
[c.] *Department of Physics, Florida A&M University, Tallahassee, FL 32307, United States*
[d.] *Department of Materials Science and Engineering, Ulsan National Institute of Science and Technology, Ulsan 44919, Republic of Korea. E-mail: hyeonjeong.lee@unist.ac.kr*
[e.] *Department of Physics, University of Central Florida, Orlando, FL 32816, United States. E-mail: shyam.kattel@ucf.edu*
† Electronic supplementary information (ESI) available. See DOI: 10.1039/x0xx00000x
‡ These authors contributed equally to this work.